

Sodium layer chiral distribution and spin structure of $\text{Na}_2\text{Ni}_2\text{TeO}_6$ with a Ni honeycomb latticeSunil K. Karna,^{1,2,*} Y. Zhao,^{3,4} R. Sankar,^{1,5} M. Avdeev,⁶ P. C. Tseng,⁷ C. W. Wang,⁸ G. J. Shu,¹
K. Matan,⁹ G. Y. Guo,^{7,10} and F. C. Chou^{1,11,12,†}¹*Center for Condensed Matter Sciences, National Taiwan University, Taipei 10617, Taiwan*²*Department of Physics & Astronomy, Louisiana State University, Baton Rouge, Louisiana 70803, USA*³*NIST Center for Neutron Research, National Institute of Standards and Technology, Gaithersburg, Maryland 20899, USA*⁴*Department of Materials Science and Engineering, University of Maryland, College Park, Maryland 20742, USA*⁵*Institute of Physics, Academia Sinica, Taipei 10617, Taiwan*⁶*Australian Nuclear Science and Technology Organisation, Locked Bag 2001, Kirrawee DC NSW 2232, Australia*⁷*Department of Physics, National Taiwan University, Taipei 10617, Taiwan*⁸*Neutron Group, National Synchrotron Radiation Research Center, Hsinchu 30076, Taiwan*⁹*Department of Physics, Faculty of Science, Mahidol University, Bangkok 10400, Thailand*¹⁰*Physics Division, National Center for Theoretical Sciences, Hsinchu 30013, Taiwan*¹¹*National Synchrotron Radiation Research Center, Hsinchu 30076, Taiwan*¹²*Taiwan Consortium of Emergent Crystalline Materials, Ministry of Science and Technology, Taipei 10622, Taiwan*

(Received 3 August 2016; revised manuscript received 31 January 2017; published 8 March 2017)

The nature of Na ion distribution, diffusion path, and the spin structure of $P2$ -type $\text{Na}_2\text{Ni}_2\text{TeO}_6$ with a Ni honeycomb lattice has been explored. The nuclear density distribution of Na ions reveals a two-dimensional (2D) chiral pattern within Na layers without breaking the original 3D crystal symmetry, which has been achieved uniquely via an inverse Fourier transform (iFT)-assisted neutron-diffraction technique. The Na diffusion pathway described by the calculated isosurface of the Na ion bond valence sum (BVS) map is found consistent to a chiral diffusion mechanism. The Na site occupancy and Ni^{2+} spin ordering were examined in detail with the neutron diffraction, magnetic susceptibility, specific heat, thermal conductivity, and transport measurements. Signatures of both strong incommensurate (ICM) and weak commensurate (CM) antiferromagnetic (AFM) spin ordering were identified in the polycrystalline sample studied, and the CM-AFM spin ordering was confirmed by using a single-crystal sample through the k scan in the momentum space corresponding to the AFM peak of $(\frac{1}{2}, 0, 1)$.

DOI: [10.1103/PhysRevB.95.104408](https://doi.org/10.1103/PhysRevB.95.104408)**I. INTRODUCTION**

The layered transition metal oxides have received special attention in condensed-matter physics research because of their rich physical properties, including ion intercalation for potential battery applications, superconductivity, and intercalant-sensitive magnetic phase transitions [1–9]. The group-IA ions that are sandwiched between the transition metal oxide layers act as passive charge reservoirs to influence the electronic structure. $P2$ -type $\text{Na}_2\text{Ni}_2\text{TeO}_6$ has been shown to exhibit high ionic conductivity at room temperature for potential applications as a separator in the Na-ion battery [10–12]. The mixed edge-sharing (Te/Ni) O_6 octahedra in each layer create a unique Te-centered Ni O_6 honeycomb lattice, which leads to a complex potential field profile that is used to drive the Na ion diffusion in two dimensions.

X-ray-diffraction studies have shown that the crystal structure of $\text{Na}_2\text{Ni}_2\text{TeO}_6$ can be indexed with a space group $P6_3/mcm$ satisfactorily, and a three-dimensional (3D) antiferromagnetic (AFM) spin ordering of $T_N \sim 27$ K has been proposed; however, the impact of Na ion diffusion on the crystal and spin structure has never been explored in detail, in contrast to its sister compound Na_xCoO_2 which has been studied extensively and shown rich physical insights [3–8,11,13,14]. It is highly desirable to investigate the 2D

structure of the Na layer that reflects the potential field generated by the (Te/Ni)-O honeycomb sublattice. In particular, due to the diffusive nature of intercalated Na ions, a unique dynamic electronic-phonon coupling of the system could be revealed through the detailed analysis of the Na ion distribution and crystal structure change as a function of temperature. Below we present an integrated synchrotron x-ray and high-resolution neutron powder-diffraction study that clearly reveals an in-plane chiral circular pattern within the Na layers. An inverse Fourier transform (iFT) technique was applied to provide real-space information from the diffraction data for a more accurate Na ion site assignment on structure refinement. Comparing to the calculated bond valence sum (BVS) map of Na, the Na-ion diffusion in two dimensions is found to follow an effective translational path of alternating chirality change.

II. EXPERIMENTAL DETAILS AND THEORETICAL CALCULATIONS

The experimental details of the polycrystalline sample preparation and single-crystal growth of $\text{Na}_2\text{Ni}_2\text{TeO}_6$ have been reported in our previous work [14]. The preliminary x-ray-diffraction measurements were performed on a Bruker D8 ADVANCE diffractometer employing $\text{Cu-}K_\alpha$ radiation, and synchrotron x-ray diffraction was performed at NSRRC using BL01C2 beam line. Neutron powder-diffraction data between 3 and 450 K were collected on the high-resolution neutron powder diffractometer (HRPD) ECHIDNA [monochromators: Ge (335), and Ge (331), $\lambda = 1.6215$ and 2.439 Å respectively]

*karnal@lsu.edu

†fcchou@ntu.edu.tw

and the high-intensity powder diffractometer (HIPD) WOM-BAT [monochromator: Ge (115) with 120° take-off angle, $\lambda = 2.9502 \text{ \AA}$], installed at the OPAL reactor in ANSTO, Australia. Approximately ~ 7 grams of the powder sample was loaded into a cylindrical vanadium can which gave rise to no measurable background diffraction peaks. Neutron-scattering experiments on powder and single-crystal samples were also conducted using the NG-5 triple-axis spectrometer SPINS at the NIST Center for Neutron Research ($\lambda = 4.702 \text{ \AA}$). A cooled beryllium filter was used to reduce the higher-order neutron contaminations. The magnetic susceptibility measurement was performed using a superconducting quantum interference device–vibrating-sample magnetometer (SQUID-VSM) (Quantum Design, USA). Chemical analysis was performed using an electron probe x-ray microanalyzer (EPMA) taken with a JEOL JXA-8200 analyzer. The bond valence sum (BVS) was calculated using the program 3DBVSMAPPER [15]. The nuclear or electron density maps were obtained employing the General Structure Analysis System (GSAS) or FULLPROF programs. Starting with the profile refinement of neutron or x-ray-diffraction pattern, the nuclear or electron-density distribution can be obtained by calculating the inverse Fourier transform of the structure factors. The scattering density $\rho(\mathbf{r}) = \frac{1}{V} \sum_{\mathbf{H}} F_{obs}(\mathbf{H}) \exp\{-2\pi i(\mathbf{H} \cdot \mathbf{r})\}$ was calculated using the program FOURIER (GSAS) or GFOURIER (FULLPROF), where V is the volume of the unit cell, \mathbf{H} is a reciprocal space vector, \mathbf{r} is a vector position inside the unit cell, and $F_{obs}(\mathbf{H}) = |F(\mathbf{H})| \exp\{i\phi(\mathbf{H})\}$, where $|F(\mathbf{H})|$ is the square root of integrated intensities taken directly from the measurement, and the calculated phase $\phi(\mathbf{H})$ derived from the structural model by the GSAS or FULLPROF program is used to perform the Fourier transform.

Theoretical calculations were performed based on first-principles density functional theory (DFT) with generalized gradient approximation (GGA) [16]. To describe the electron-electron correlation associated with the $3d$ states of Ni, the GGA plus on-site Coulomb repulsion (GGA + U) calculations are performed with an effective $U_{\text{eff}} = (U - J) = 6.0 \text{ eV}$ [17,18]. We have used the frozen-core full-

potential projector-augmented wave (PAW) method [19,20] as implemented in the Vienna *ab initio* simulation package (VASP) [21]. The wave functions are expressed in a plane-wave basis set with an energy cutoff of 400 eV, and the self-consistent field energies are converged up to 10^{-5} eV . For our calculations, we have used four metastable magnetic configurations to estimate the magnetic couplings J_1 , J_2 , and J_3 of Ni atoms of interatomic distances 3.002, 5.200, and 5.564 \AA (the three shortest interatomic distances) respectively. To explore the magnetic ground state, a supercell four times the size of a primitive cell is considered, and there are 16 Ni atoms in the unit cell. In the present calculations, we used the tetrahedron method with Blöchl corrections for the Brillouin-zone integration with a Γ -centered Monkhorst-Pack k -point mesh of $(9 \times 9 \times 7)$. The magnetic couplings J_1 , J_2 , and J_3 among the Ni atoms are expressed in terms of the spin Heisenberg Hamiltonian, $H = E_0 - \sum J_{ij} \mathbf{S}_i \cdot \mathbf{S}_j$, where J_{ij} is the exchange interaction parameter between the Ni atoms at site i and site j , and \mathbf{S}_i (\mathbf{S}_j) is the unit vector that represents the direction of the local magnetic moment at site i (j). For an antiferromagnetic interaction, $J < 0$ is assumed, and for a ferromagnetic interaction, $J > 0$ is assumed, and the constant E_0 contains all of the spin-independent interactions.

III. RESULTS AND DISCUSSION

A. Crystal structure

The crystalline structure of $\text{Na}_2\text{Ni}_2\text{TeO}_6$ can be viewed as a 2D honeycomb lattice that is composed of edge-sharing NiO_6 octahedra with TeO_6 in each honeycomb center, and the Na monolayer is sandwiched between two (Ni/Te)-O layers with mirrored orientations along the a axis in each unit cell, as shown in Fig. 1. Based on the x-ray-diffraction results, Evstigneeva *et al.* indexed the diffraction pattern with a space group of $P6_3/mcm$ using three crystallographic sites of Na1 at $6g$ ($0.35, 0, \frac{1}{4}$), Na2 at $4c$ ($\frac{1}{3}, \frac{2}{3}, \frac{1}{4}$), and Na3 at $2a$ ($0, 0, \frac{1}{4}$), with corresponding occupancies of 44%, 21%, and 25%, respectively [11]. In this study, neutron diffraction was applied to elucidate the Na ion positions and their corresponding

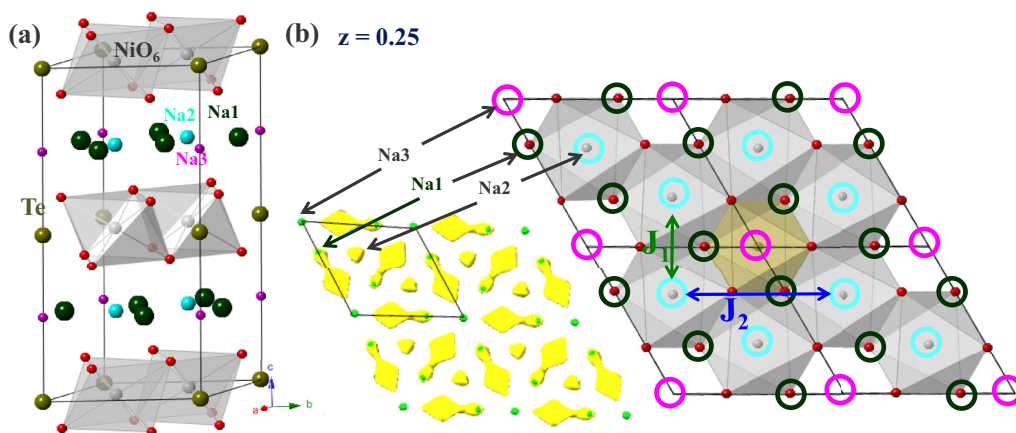


FIG. 1. (a) The crystal structure of $\text{Na}_2\text{Ni}_2\text{TeO}_6$ of space group $P6_3/mcm$ with three major Na sites (Na1, Na2, and Na3) assigned following Ref. [11]. (b) The 2D honeycomb lattice is composed of edge-shared NiO_6 with Te (also edge-shared TeO_6 octahedron) sitting in each honeycomb center, with Na sites in the neighboring layer shown as circles. The electron-density map obtained from the iFT-assisted x-ray diffraction at $z = 0.25$ is shown on the left. The effective magnetic exchange couplings J_1 and J_2 are indicated.

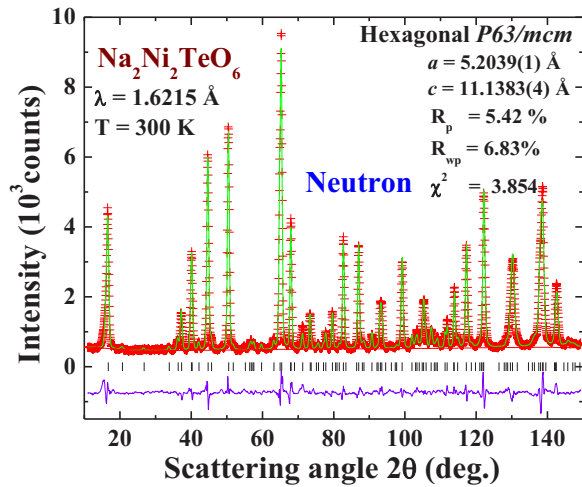


FIG. 2. Observed (crosses) and fitted (solid lines) high-resolution neutron powder-diffraction patterns taken at 300 K, assuming a hexagonal crystal structure with the $P6_3/mcm$ space group. The differences between the calculated and observed patterns are plotted at the bottom. The solid vertical lines mark the calculated positions of the Bragg reflections of the proposed crystalline structure.

occupancies more precisely. The high-resolution neutron powder-diffraction (NPD) data were refined with the Rietveld method using the General Structure Analysis System (GSAS) program [22,23].

The refinements were performed assuming a hexagonal crystal structure with space group $P6_3/mcm$. Figure 2 displays the observed (crosses) and calculated (solid lines) diffraction patterns taken at 300 K, with differences plotted at the bottom. The nuclear density of the Na layer at $z = 0.25$ is represented with a map that takes a 0.2-Å-thick cut from the 3D real-space view, which is reconstructed from the diffraction data via an inverse Fourier transform (iFT), as displayed in Figs. 3(a)–3(c). It is noted that the original assignments of the Na1, Na2, and Na3 sites do not match the iFT-assisted real-space crystal structure of the Na layer perfectly. A better site assignment should reflect the additional Na sites that are revealed by the iFT technique, as indicated by the quintuplet splitting of Na1($a-e$), the triplet splitting of Na2($a-c$), and the doublet splitting of Na3($a-b$). All corresponding occupancies are summarized in Table I. The newly assigned Na sites are overlaid to match the nuclear density mapping more satisfactorily, as shown in Fig. 3(a).

It must be noted that these Na sites from the iFT-assisted NPD data refinement do not offer additional 3D symmetry breaking from the original space group $P6_3/mcm$. In addition, similar iFT-assisted x-ray-diffraction data analysis showing electron density distribution [inset of Fig. 1(b)] is not sufficiently sensitive to resolve the Na sites of low occupancy, which makes current iFT-assisted NPD data analysis a unique and necessary method for the accurate site refinement of the temperature and potential field-sensitive diffusive Na ions.

B. Sodium distribution and diffusion

Following the iFT-assisted NPD data analysis, the experimental nuclear density mapping revealed a circular pattern

of well-defined handedness in the Na layer, as illustrated in Figs. 3(a)–3(c). A chiral circular pattern can be identified from the nuclear density distribution of the Na1($a-e$) sites surrounding the Na2 a center in circles showing alternating handedness (counterclockwise and clockwise). The observed 2D chiral pattern has also been confirmed by the electron-density mapping using x-ray diffraction with the similar iFT-assisted data analysis [inset of Fig. 1(b)], wherein the electron density (not the nuclear density) distribution of the unresolved Na1 sites indeed shows an in-plane (2D) chiral pattern similar to that identified by the iFT-assisted NPD data [Fig. 3(a)]. Such a chiral pattern in two dimensions does not break the 3D symmetry, but its role in 2D symmetry cannot be dismissed completely. For example, such a unique local chiral element is found in chiral molecules distributed in two dimensions [24]. The unique chiral element (or named chiral asymmetry) would reduce the 2D symmetry from $p3m1$ (no. 14) to $p3$ (no. 13) within the classification of 17 2D (wallpaper) space groups.

Although a unique potential field reversal is expected between the (Ni/Te)-O layers following the symmetry operation with the space group $P6_3/mcm$, such an in-plane chiral pattern cannot be assigned unambiguously with the parameters of the anisotropic B factor alone, as indicated by the B factors listed in Table I. It is noted that a distinct chiral pattern can also be identified by applying the iFT-assisted NPD data analysis using the primitive space group $P1$ (no. 1) without adding a presumed symmetry operation for a hexagonal system, as shown in Fig. 3(d); i.e., the observed chirality is intrinsic and not an artifact generated by the choice of space group used in the iFT operation.

In view of $\text{Na}_2\text{Ni}_2\text{TeO}_6$ as a layered compound with Na ions intercalated in the van der Waals (vdW) gap, the nuclear density distribution shown in Fig. 3 could be interpreted as the time-averaged Na ion distribution influenced by the electric potential field, and the potential field is constructed by the neighboring (Ni/Te)-O layers under thermal fluctuation. This assumption has been supported by the calculated Na ion diffusion path from the molecular dynamic simulations performed earlier [25]. The isosurface of the Na bond valence sum (Na-BVS) map shown in Fig. 4 is calculated from the difference between the experimentally calculated Na-BVS and the ideal valence of $+1(\pm 0.2)$ for the Na ion [15]. The BVS isosurface network is continuous across the Na1($c-e$) and Na2($a-c$) multiplet sites within the Na layer, but leaves out the Na1($a-b$) and Na3($a-b$) sites completely, as shown in Fig. 4(a), which suggests that a Na-ion diffusion path in two dimensions is established following the Na1($c-e$)-Na2($a-c$) sites in a circular manner. A similar Na diffusion path has also been reported earlier in $\text{Na}_{0.7}\text{CoO}_2$ and $\text{Na}_3[\text{Ti}_2\text{P}_2\text{O}_{10}\text{F}]$ via the mean-square displacements and thermal ellipsoid calculations respectively [7,26].

It is instructive to examine the Na distribution as a function of temperature for the Na site occupancies in detail, as shown in Fig. 4(b). Na1($c-e$) shows nearly twice the integrated occupancy as that of Na2($a-c$) at 300 K, but there is an additional weight shift of approximately 2% of the occupancy from Na2($a-c$) to Na1($c-e$) between ~ 220 and 150 K. On the other hand, the occupancies of Na1($a-b$) and Na3($a-b$) remain low and constant in the same temperature range. The actual Na

TABLE I. List of the refined structural parameters of $\text{Na}_2\text{Ni}_2\text{TeO}_6$ at 300 K, based on the assigned Na positions similar to those reported in the literature by Evstigneeva *et al.*, and the iFT-assisted refinement from this study (lower), where B_{iso} represents the isotropic temperature parameter and M represents the multiplicity.

$\text{Na}_2\text{Ni}_2\text{TeO}_6$						
Hexagonal $P6_3/mcm$ space group (no. 193)						
$T = 300 \text{ K}, a = b = 5.2036(3) \text{ \AA}, c = 11.1387(3) \text{ \AA}$						
Atom	x	y	z	M	$B_{iso} (\text{\AA}^2)$	Occupancy
Te	0	0	0	2a	0.19(3)	1.000
Ni	$\frac{2}{3}$	$\frac{1}{3}$	0	4c	0.30(2)	0.997(3)
O	0.3112(2)	0.3112(2)	0.5944(1)	12b	0.57(4)	1.002(3)
Na1	0.6306(3)	0.0	$\frac{1}{4}$	6g	4.98(5)	0.508(4)
Na2	$\frac{1}{3}$	$\frac{2}{3}$	$\frac{1}{4}$	4c	3.12(3)	0.203(2)
Na3	0	0.0	$\frac{1}{4}$	2a	2.88(3)	0.073(1)
$\chi^2 = 5.654, R_p = 6.92\%, R_{wp} = 8.81\%$						
$\text{Na}_2\text{Ni}_2\text{TeO}_6$						
Hexagonal $P6_3/mcm$ space group (no. 193)						
$T = 300 \text{ K}, a = b = 5.2039(1) \text{ \AA}, c = 11.1383(4) \text{ \AA}$						
Atom	x	y	z	M	$B_{iso} (\text{\AA}^2)$	Occupancy
Te	0	0	0	2a	0.18(5)	1.000
Ni	$\frac{2}{3}$	$\frac{1}{3}$	0	4c	0.28(4)	1.003(2)
O	0.3112(2)	0.3112(2)	0.5943(1)	12b	0.57(6)	0.992(2)
Na1a	0.3538(4)	0.0	$\frac{1}{4}$	6g	2.28(4)	0.012(2)
Na1b	0.415(3)	0.072	$\frac{1}{4}$	6g	2.28(4)	0.051(3)
Na1c	0.6250(5)	0.0	$\frac{1}{4}$	6g	6.74(7)	0.038(2)
Na1d	0.6921(5)	0.065	$\frac{1}{4}$	6g	6.74(7)	0.165(2)
Na1e	0.6252(2)	0.1042(3)	$\frac{1}{4}$	12j	0.91(2)	0.018(1)
Na2a	$\frac{1}{3}$	$\frac{2}{3}$	$\frac{1}{4}$	4c	1.44(3)	0.103(3)
Na2b	0.5639(4)	0.1872(1)	$\frac{1}{4}$	12j	0.91(1)	0.013(4)
Na2c	0.6881(2)	0.2190(4)	$\frac{1}{4}$	12j	3.71(2)	0.014(2)
Na3a	0	0.0	$\frac{1}{4}$	2a	1.60(4)	0.043(1)
Na3b	0.8570(4)	0.0	$\frac{1}{4}$	6g	4.37(3)	0.012(3)
$\chi^2 = 3.854, R_p = 5.42\%, R_{wp} = 6.83\%$						

diffusion path is thus hinted by the gradual weight shift of the occupancy between Na1($c-e$) and Na2($a-c$) experimentally, in agreement with the prediction of BVS calculation. In addition, it is suggested that Na diffusion occurs above $\simeq 220$ K but falls to the relative ground state below $\simeq 150$ K, which is consistent to the freezing phenomenon of Na observed in the layered Na_xCoO_2 below ~ 150 K via ^{23}Na NMR [5,27].

Since the Na1($c-e$) \leftrightarrow Na2($a-c$) diffusion path (Fig. 4) forms closed loops in 2D close packing, a purely rotational diffusion is likely. In order to introduce an effective translational diffusion, the possible purely rotational diffusion can be avoided by coupling the rotation to an orientational diffusion, as demonstrated by the chiral diffusion for a system of rotary nanomotors [28]. The revealed chiral circular pattern in two dimensions must help in making $\text{Na}_2\text{Ni}_2\text{TeO}_6$, a compound of high ionic conductivity.

C. Magnetic phase transitions

The AFM phase transition for $\text{Na}_2\text{Ni}_2\text{TeO}_6$ was verified with elastic neutron scattering using both powder and single-

crystal samples through the trace of superlattice peaks as a function of the temperature, as shown in Fig. 5(a). At $T = 5$ K, a commensurate (CM) superlattice peak at (0.5 0 1) and a broad incommensurate (ICM) superlattice peak near $\mathbf{k} = (0.47 \ 0.44 \ 0.28)$ can be identified in the powder sample. While the observed ICM peak has a shoulder close to a possible CM peak of (0.5 0 0) and the ICM peak cannot be deconvoluted with confidence due to the limited instrumental resolution, the peak intensities are plotted as a function of temperature to show that both CM and ICM peaks have the same onset at T_N of ~ 27.5 K, as shown in Fig. 5(b), which has also been identified by the distinct cusp shown in the $d\chi/dT$ and C_p/T plots [see Fig. 5(c)]. Similar CM propagation vector $k = (0.5 \ 0 \ 0)$ has recently been proposed in the isostructural $\text{Na}_2\text{Co}_2\text{TeO}_6$ compound [29]. Our preliminary single-crystal studies indicated that the T_N is extremely sensitive to the excess Na content, e.g., $T_N \sim 22$ K has been identified in a single-crystal sample of Na content ~ 2.16 [30]. A separate spin-polarized neutron experiment is required to elucidate the relationship among the Na content and ICM/CM spin structures further.

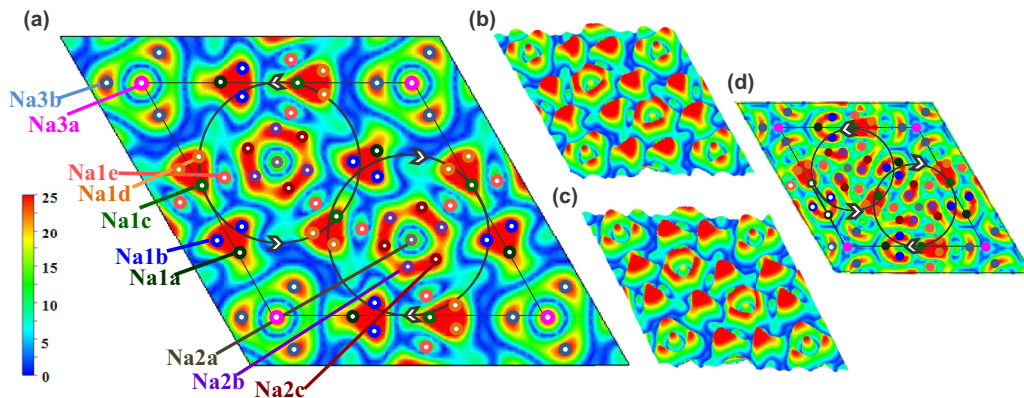


FIG. 3. (a) The nuclear density map for $\text{Na}_2\text{Ni}_2\text{TeO}_6$ at $z = 0.25$ is overlaid with Na sites obtained from the iFT-assisted NPD data refinement, which indicates additional Na1-quintuplet, Na2-triplet, and Na3-doublet splittings are required for the space group $P6_3/mcm$, and the corresponding site occupancies are summarized in Table I. The corresponding 3D contour maps at layers (b) $z = 0.25$ and (c) $z = 0.75$ are compared. The nuclear densities of $\text{Na}1a$ – $\text{Na}1d$ sites are shown with opposite handedness surrounding the $\text{Na}2a$ center between the neighboring Na layers also. (d) Similar handedness can also be identified with space group $P1$ without any presumed symmetry in the hexagonal system, as shown for the $z = 0.25$ plane via iFT-assisted data analysis using the same NPD data.

We have tentatively explored the CM superlattice peak at $(0.5\ 0\ 1)$ using a separate single-crystal sample, as shown by the H - L contour plot of the $(0.5\ 0\ 1)$ peak intensity [inset of Fig. 5(a)] at 5 K. The critical exponent of $\beta = 0.202$ fitted from the powder sample ICM peak intensity with $(1 - T/T_N)^{2\beta}$ [Fig. 5(b)] suggests the 2D nature of the observed phase transition, which is consistent with the evolution of a short-range exchange coupling prior to the 3D long-range spin ordering, as also revealed by the broad $\chi(T)$ peak near ~ 30 – 40 K right above T_N (lower inset of Fig. 7).

D. Magnetic structure calculations

Judging from the $\chi_{\parallel c}(T < T_N)$ drop to indicate the on-site spin anisotropy along the c direction [14], we have considered

four possible magnetic configurations to evaluate the three spin exchange parameters based on the first-principle density functional theory with a generalized gradient approximation (GGA) [16], including an antiferromagnetically coupled ferromagnetic (FM) zigzag chain structure (AF1), a $q = 0$ spin configuration for each honeycomb sublattice (AF2), an A-type AFM spin structure similar to that found in $\text{Na}_{0.82}\text{CoO}_2$ (AF3) [31], and a FM spin structure were calculated, as illustrated in Figs. 6(b)–6(e). The explicit relations between the energy and exchange coupling parameters for the proposed configurations are $E_{AF1} = E_0 - 8J_1 + 16J_2 + 16J_3$, $E_{AF2} = E_0 + 8J_1 - 16J_2 + 16J_3$, $E_{AF3} = E_0 - 24J_1 - 48J_2 + 16J_3$, and $E_{FM} = E_0 - 24J_1 - 48J_2 - 16J_3$. Considering the in-plane nearest-neighbor couplings of J_1 (Ni-O-Ni) through the superexchange route and the next-nearest-neighbor

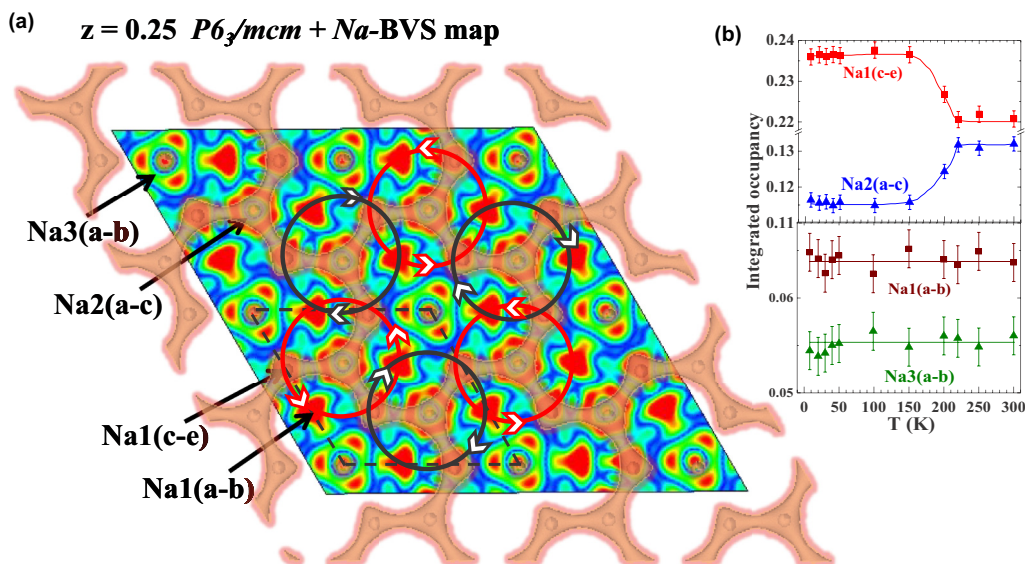


FIG. 4. (a) The nuclear density map of the $z = 0.25$ layer cut for $\text{Na}_2\text{Ni}_2\text{TeO}_6$ at 300 K, obtained using iFT-assisted NPD data via space group $P6_3/mcm$, where the calculated BVS iso-surface (in brown color) of Na ions is overlaid on top. (b) The temperature dependence of the integrated Na1-Na2-Na3 site occupancies. Solid lines are a guide to the eye.

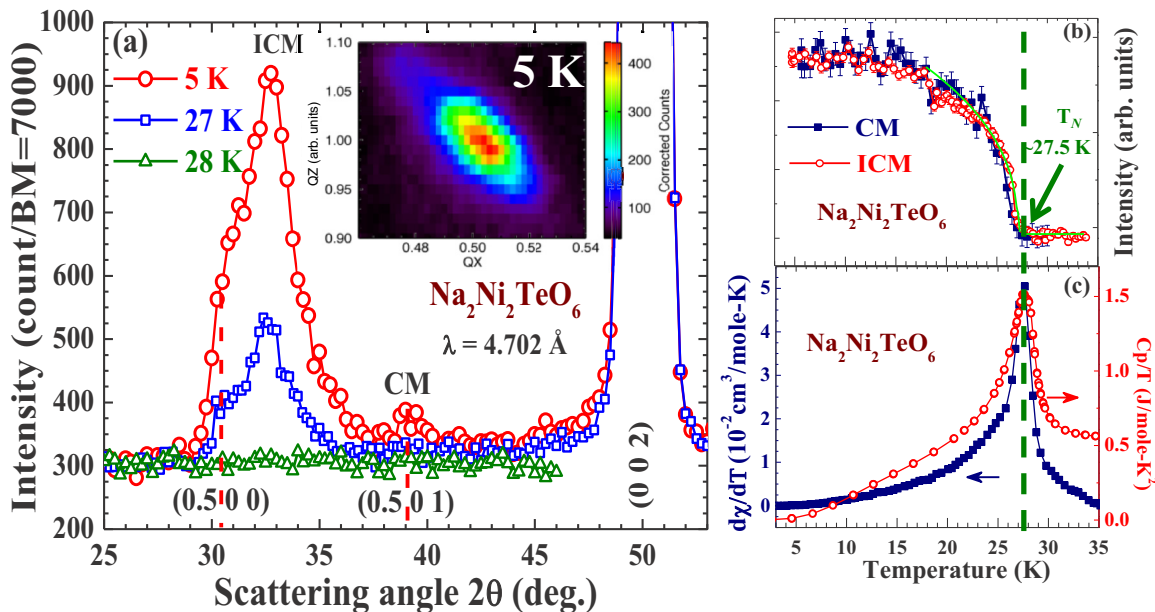


FIG. 5. (a) CM and ICM AFM peaks observed in the powder sample of $\text{Na}_2\text{Ni}_2\text{TeO}_6$ below 28 K. (b) Thermal variations of ICM and CM peaks indicate an onsets of $T_N \sim 27.5 \text{ K}$. (c) The $d\chi/dT$ and C_p/T plots also indicate an anomaly near $\sim 27.5 \text{ K}$.

coupling J_2 (Ni-O...O-Ni) through the supersuperexchange route [Fig. 1(b)], and an interplane coupling of J_3 , the magnetic ground state is calculated to be the spin configuration of the antiferromagnetically coupled FM zigzag chains (AF1), as illustrated in Fig. 6(a). The calculated values for the ground state are found to be $E_0 = -451.37 \text{ eV/unit cell}$, $J_1 = 0.2 \text{ meV}$, $J_2 = -1.2 \text{ meV}$, and $J_3 = -0.1 \text{ meV}$, as listed in Table II. As a check for the validity of calculations, a mean-field estimate of Weiss temperature Θ based on the

calculated exchange coupling parameters gives $\Theta \sim -26 \text{ K}$, being in good agreement with the experimental value of -32 K obtained from the Curie-Weiss law fitting [32,33].

It is noted that the definition of a Ni $S = 1$ spin chain in the 2D honeycomb lattice is ambiguous when three equivalent zigzag chains can be defined along the $(1\ 0\ 0)$, $(0\ 1\ 0)$, and $(1\ 1\ 0)$ directions of a hexagonal system. According to the experimental and theoretical information collected to date, including the identification of the AFM peak $(\frac{1}{2}\ 0\ 1)$,

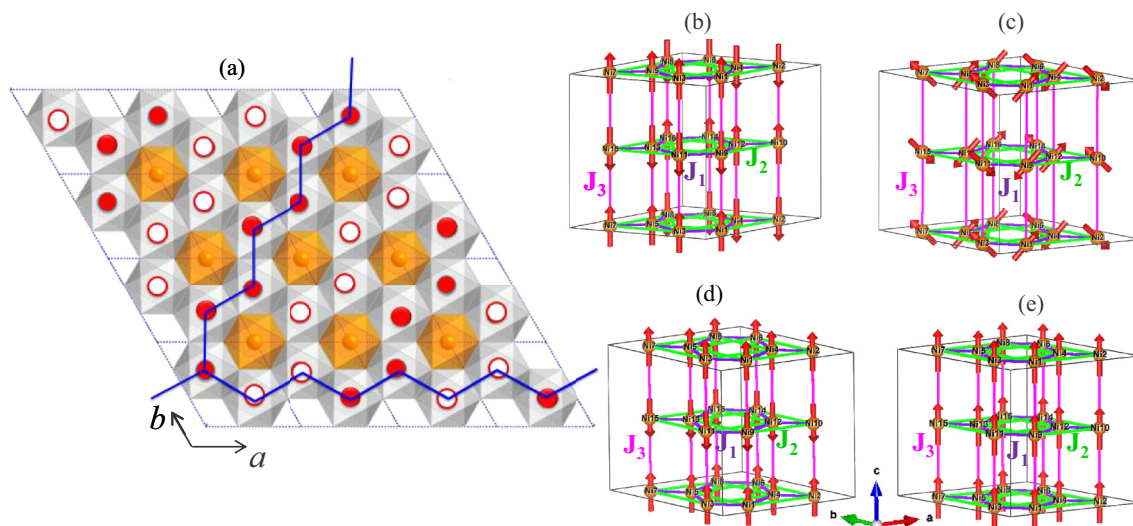


FIG. 6. (a) The proposed commensurate AFM spin structure in two dimensions, where solid and empty circles represent spins up and down respectively. Zigzag chains with doubled periodicity along the a direction is indicated by the blue lines, which can also be viewed as antiferromagnetically coupled FM zigzag chains extending along the (110) direction. (b)–(e) Four possible spin configurations for the theoretical ground-state calculation. The proposed spin configuration shown in (b) is found to be identical and can be described equivalently using spin dimers in linear chain along the a or b direction after a 60° axis transformation within the ab plane, as shown in (a). (b) Configuration 1 (AF coupled FM zigzag chains), (c) Configuration 2 ($q = 0$ spin configuration for honeycomb lattice), (d) Configuration 3 (A-type AF spin structure) and (e) Configuration 4 (FM spin structure).

TABLE II. Calculated exchange energies for J_1 (Ni-O-Ni) and J_2 (Ni-O...O-Ni) as illustrated in Fig. 1(b) with interplane coupling J_3 , where $J < 0$ is assumed for the AFM coupling.

	J_1	J_2	J_3
J_i (meV)	0.2	-1.2	-0.1
J_i (K)	1.70	-13.47	-0.87
Ni-Ni distance (Å)	3.002	5.200	5.564

the confirmed 3D AFM spin ordering, the spin anisotropy along the c direction [14], and the theoretically calculated ground-state configurations [Figs. 6(b)–6(e)] of dominant next-nearest-neighbor AFM coupling J_2 with weak-nearest-neighbor FM coupling J_1 , a commensurate AFM spin structure is proposed and shown in Fig. 6(a). This proposed spin structure satisfies all of the experimental and theoretical conditions for the confirmed AFM long-range spin ordering, with a doubled lattice size along the equivalent a and b directions of the hexagonal lattice.

Although the AFM long-range spin ordering is expected to coincide with the lattice size doubling along the c direction of opposite handedness in the Na layer, strong ICM peaks were identified in the powder sample [Fig. 5(a)], which could have resulted from the incommensurate modulation of the AFM spin arrangement of a 3D helical spin ordering. While the chiral symmetry is closely related to the Coulomb field that is revealed by the nuclear density distribution of the Na layer, the observed incommensurability could be closely related to the oxygen and/or Na nonstoichiometry. Preliminary chemical analysis using electron probe microanalysis (EPMA) suggests that the studied powder sample has an oxygen vacancy level about ~ 0.02 per formula unit. A careful neutron study on a series of single-crystal samples with controlled oxygen and Na nonstoichiometry is expected and in progress.

E. Spin-phonon-electronic coupling

The lattice parameters a and c for $\text{Na}_2\text{Ni}_2\text{TeO}_6$ measured as a function of the temperature are shown in Fig. 7. No structural symmetry change or lattice distortion could be identified from the high-resolution neutron powder-diffraction patterns between 3 and 450 K. The thermal expansion was essentially isotropic above ~ 220 K, as indicated by the linear temperature dependence. The calculated thermal-expansion coefficients are $\alpha_a = 9.78 \times 10^{-6} \text{ K}^{-1}$ along the a axis and $\alpha_c = 2.62 \times 10^{-5} \text{ K}^{-1}$ along the c axis for data above ~ 200 K. The α_c is approximately 2.68 times higher than α_a , which indicates that the interlayer coupling is considerably weaker than that of the intralayer coupling, as expected for a layered compound with vdW gaps.

The temperature range for the occurrence of the zero-thermal-expansion (ZTE) phenomenon below ~ 100 K is found close to the onset that $\chi(T)$ starts to deviate from the Curie-Weiss law (lower right inset of Fig. 7), indicating both the anharmonic phonon contribution and the short-range spin exchange coupling are required as the precursor to the 3D long-range spin ordering below $T_N \sim 27.5$ K. These findings are consistent with a picture of the dominant spin-phonon coupling under reduced thermal fluctuation. The onset of

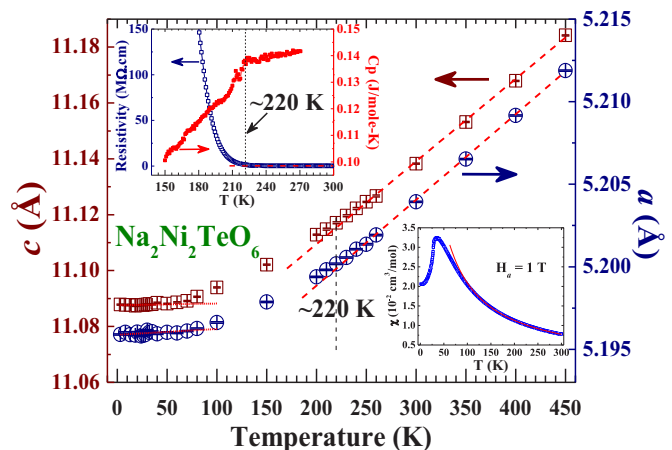


FIG. 7. The temperature dependence of the lattice parameters a and c for $\text{Na}_2\text{Ni}_2\text{TeO}_6$. The linear temperature dependence is found to be above ~ 220 K, and the ZTE phenomenon is found to be below ~ 100 K. The upper left inset shows anomalies in the specific heat and resistivity of $\text{Na}_2\text{Ni}_2\text{TeO}_6$ near ~ 220 K. The lower right inset shows the temperature dependence of magnetic susceptibilities for powder $\text{Na}_2\text{Ni}_2\text{TeO}_6$ measured in the applied field of $H_a = 1$ T. The solid line represents the Curie-Weiss law fitting.

linear thermal expansion near ~ 220 K was also found near the temperature range where the Na1/Na2 occupancies start to switch weights [Fig. 4(b)], which suggests that the subtle in-plane chirality must be closely related to the electron-phonon coupling indicated by the cusp of specific heat C_p and the onset of resistivity increase near ~ 220 K (upper left inset of Fig. 7). Clearly, it is the diffusive nature of the Na valence electron that makes the observation of all these correlated phenomena possible.

F. 2D chirality and 3D spin ordering

We believe that the hidden chirality in the Na layer results from the electric potential gradient created by the neighboring Ni-O layers, which is supported by the detected significant $(h,k,l \neq 0)$ peak broadening due to strain calculated using the FULLPROF suite [34] in Table III, in contrast to the narrow $(h,k,l = 0)$ peaks which are within the instrumental resolution (Fig. 8). The different type of bonding between the weaker interlayer van der Waals interaction and the stronger intralayer covalent bonding could be responsible for

TABLE III. Strain calculated for various diffraction peaks shown in the neutron-diffraction pattern. Strain is estimated using FULLPROF suite from the integral peak width β and the d spacing as $\frac{1}{2}\beta d$.

HKL	HG_o	HG_i	Strain
(1 0 0)	0.4025	0.4267	resolution limited
(1 0 2)	0.4232	0.4111	21.7251
(3 0 0)	0.3141	0.3390	resolution limited
(1 1 6)	0.7227	0.3383	22.0218
(3 0 2)	0.4909	0.3498	11.0855
(1 1 2)	0.4116	0.3762	16.8185
(2 1 1)	0.3426	0.3375	6.7922

TABLE IV. DFT calculations of exchange couplings J_1 , J_2 , J_3 for three different types of Na occupancy distribution are compared.

Occupancies	$J_1/J_2/J_3$		
	100% Na2	62.5% Na1, 37.5% Na2	100% Na1
J_i (meV)	0.15/-1.16/-0.08	-0.11/-1.12/-0.07	-0.06/-1.13/-0.05
J_i (K)	1.70/-13.47/-0.87	-1.31/-12.96/-0.83	-0.66/-13.08/-0.54

the tolerable anisotropic displacement of oxygen atoms under thermal fluctuation, and the detected strain reflects the required potential gradient for the Na ion diffusion following the Fick's second law [13]. Above all, the chirality displayed by the Na ion distribution is hidden in the regular refinement that considers the statistical atomic position only.

In order to test the impact of Na chiral distribution on the spin ordering, DFT calculations of exchange couplings J_1 - J_2 - J_3 for systems having three different site occupancy assignments are compared, from calculation using the refined occupancies of 62.5% Na1/37.5% Na2 to the fully

occupied Na2 and Na1, as shown in Table IV. It is found that the dominant J_2 is not affected significantly by the occupancy change, but the weak J_1 and J_3 couplings are reduced accordingly. Based on these simulated calculations, we propose that the observed Na-layer 2D chiral distribution via weighted multiplet splitting cannot affect the magnetic couplings significantly.

While the in-plane antiferromagnetically coupled spin chains [see Fig. 6(a)] may break the mirror symmetry of the honeycomb lattice via an expected Peierls-like AFM interchain coupling, current neutron and x-ray structure analysis failed to detect the expected mirror symmetry breaking; instead, an in-plane chirality was uniquely identified in the Na layer. It is likely that the 2D chiral distribution pattern identified in the Na layer may induce the structure relaxation via phonon softening only without breaking the original 3D crystal symmetry.

IV. CONCLUSIONS

In summary, we have investigated the 2D structure of the Na layer that reflects the potential field generated by the (Te/Ni)-O honeycomb sublattice. This system exhibits Na diffusion behavior at higher temperatures above ~ 220 K but ceases at lower temperatures. The diffusion has been reflected in the thermal variations of Na occupancy, transport, and specific-heat measurements through the identical onsets of ~ 220 K for the corresponding 2% weight shift in Na occupancy, resistivity increase, and broad specific heat anomaly; in other words, a weak exothermic phase transition for the Na ion ordering in progress is disclosed. The iFT-assisted powder neutron-diffraction refinement technique is crucial to provide an accurate site refinement for the diffusive Na ions in the layered material like $\text{Na}_2\text{Ni}_2\text{TeO}_6$. A chiral distribution pattern hidden in the Na layer is found to be intimately related to its diffusion behavior and shows significant phonon-electronic coupling.

ACKNOWLEDGMENTS

F.C.C. acknowledges support funded by the Ministry of Science and Technology (MOST), Taiwan under Project No. 103-2119-M-002-020-MY3 and the neutron group of National Synchrotron Radiation Research Center (NSRRC), Taiwan under MOST Project No. 103-2739-M-213-001-MY3. We acknowledge the support of the ANSTO and NIST for providing the neutron beam time that made the neutron-scattering measurements possible. The identification of any commercial product or trade name does not imply endorsement or recommendation by National Institute of Standards and Technology.

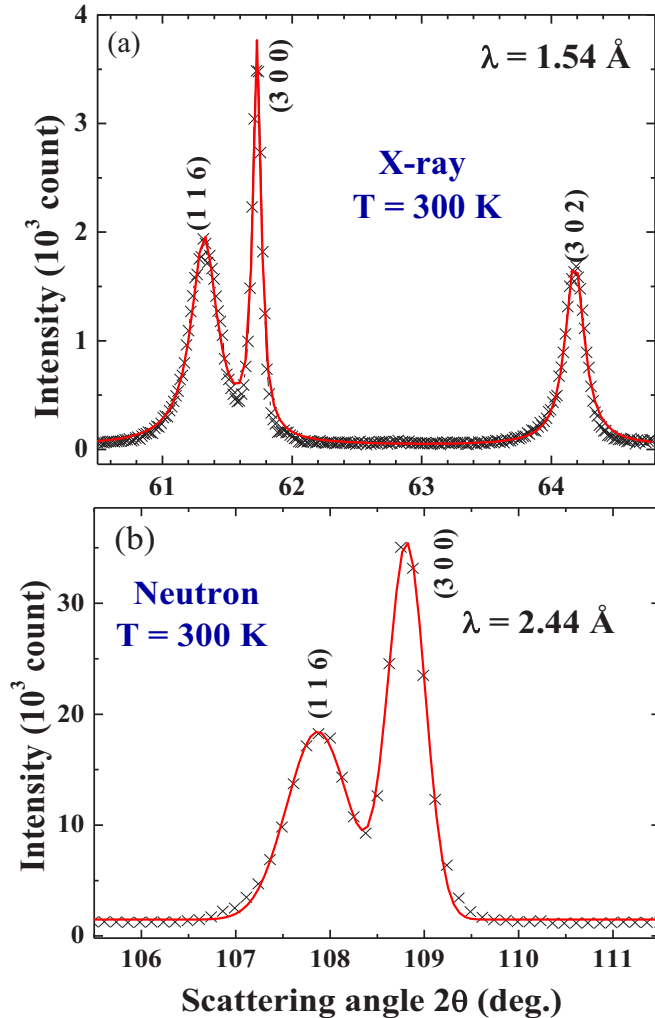


FIG. 8. A portion of the fitted (a) x-ray and (b) neutron-diffraction patterns showing $l \neq 0$ peaks broadening and $l = 0$ peaks with full width at half maximum within the instrumental resolution. All $\text{Cu-K}\alpha_2$ for the x-ray has been filtered out. The calculated corresponding strain is tabulated in Table III.

- [1] I. Terasaki, Y. Sasago, and K. Uchinokura, *Phys. Rev. B* **56**, R12685 (1997).
- [2] R. E. Schaak, T. Klimczuk, M. L. Foo, and R. J. Cava, *Nature (London)* **424**, 527 (2003).
- [3] M. Lee, L. Viciu, L. Li, Y. Wang, M. L. Foo, S. Watauchi, R. A. Pascal, Jr, R. J. Cava, and N. P. Ong, *Nat. Mater.* **5**, 537 (2006).
- [4] G. J. Shu and F. C. Chou, *Phys. Rev. B* **93**, 140402(R) (2016).
- [5] M. Weller, A. Sacchetti, H. R. Ott, K. Mattenberger, and B. Batlogg, *Phys. Rev. Lett.* **102**, 056401 (2009).
- [6] R. Berthelot, D. Carrier, and C. Delmas, *Nat. Mater.* **10**, 74 (2011).
- [7] M. Medarde, M. Mena, J. L. Gavilano, E. Pomjakushina, J. Sugiyama, K. Kamazawa, V. Yu. Pomjakushin, D. Sheptyakov, B. Batlogg, H. R. Ott, M. Månsson, and F. Juranyi, *Phys. Rev. Lett.* **110**, 266401 (2013).
- [8] G. J. Shu and F. C. Chou, *Phys. Rev. B* **88**, 155130 (2013).
- [9] *Linden's Handbook of Batteries*, 4th ed., edited by D. Linden and T. B. Reddy (McGraw-Hill Inc., New York, 2010).
- [10] R. Berthelot, W. Schmidt, A. W. Sleight, and M. A. Subramanian, *J. Solid State Chem.* **196**, 225 (2012).
- [11] M. A. Evstigneeva, V. B. Nalbandyan, A. A. Petrenko, B. S. Medvedev, and A. A. Kataev, *Chem. Mater.* **23**, 1174 (2011).
- [12] A. Gupta, C. B. Mullins, and J. B. Goodenough, *J. Power Sources* **243**, 817 (2013).
- [13] G. J. Shu and F. C. Chou, *Phys. Rev. B* **78**, 052101 (2008).
- [14] R. Sankar, I. P. Muthuselvam, G. J. Shu, W. T. Chen, S. K. Karna, R. Jayavel, and F. C. Chou, *CrystEngComm* **16**, 10791 (2014).
- [15] M. Sale and M. Avdeev, *J. Appl. Crystallogr.* **45**, 1054 (2012).
- [16] J. P. Perdew, K. Burke, and M. Ernzerhof, *Phys. Rev. Lett.* **77**, 3865 (1996).
- [17] S. L. Dudarev, G. A. Botton, S. Y. Savrasov, C. J. Humphreys, and A. P. Sutton, *Phys. Rev. B* **57**, 1505 (1998).
- [18] A. Jain, G. Hautier, S. P. Ong, C. J. Moore, C. C. Fischer, K. A. Persson, and G. Ceder, *Phys. Rev. B* **84**, 045115 (2011).
- [19] P. E. Blochl, *Phys. Rev. B* **50**, 17953 (1994).
- [20] G. Kresse and D. Joubert, *Phys. Rev. B* **59**, 1758 (1999).
- [21] G. Kresse and J. Hafner, *Phys. Rev. B* **47**, 558 (1993).
- [22] A. C. Larson and R. B. von Dreele: General Structure Analysis System Report No. LA-UR-86-748, Los Alamos National Laboratory, 2004.
- [23] H. M. Rietveld, *J. Appl. Crystallogr.* **2**, 65 (1969).
- [24] J. A. A. W. Elemans, I. De Cat, H. Xua, and S. De Feyter, *Chem. Soc. Rev.* **38**, 722 (2009).
- [25] K. Sau and P. P. Kumar, *J. Phys. Chem. C* **119**, 1651 (2015).
- [26] Z. Ma, Y. Wang, C. Sun, J. A. Alonso, M. T. Fernández-Díaz, and L. Chen, *Sci. Rep.* **4**, 7231 (2014).
- [27] T. F. Schulze, P. S. Häfliger, Ch. Niedermayer, K. Mattenberger, S. Bubenhofer, and B. Batlogg, *Phys. Rev. Lett.* **100**, 026407 (2008).
- [28] A. Nourhani, P. E. Lammert, A. Borhan, and V. H. Crespi, *Phys. Rev. E* **87**, 050301(R) (2013).
- [29] E. Lefrançois, M. Songvilay, J. Robert, G. Nataf, E. Jordan, L. Chaix, C. V. Colin, P. Lejay, A. Hadj-Azzem, R. Ballou, and V. Simonet, *Phys. Rev. B* **94**, 214416 (2016).
- [30] S. K. Karna, Y. Zhao, R. Sankar, M. Avdeev, C. W. Wang, and F. C. Chou (unpublished).
- [31] S. P. Bayrakci, I. Mirebeau, P. Bourges, Y. Sidis, M. Enderle, J. Mesot, D. P. Chen, C. T. Lin, and B. Keimer, *Phys. Rev. Lett.* **94**, 157205 (2005).
- [32] J. S. Smart, *Effective Field Theory of Magnetism* (Saunders, Philadelphia, 1996).
- [33] P. W. Anderson, in *Solid State Physics*, edited by F. Seitz and D. Turnbull (Academic, New York, 1963), Vol. 14, pp. 99–214.
- [34] J. Rodriguez-Carvajal, *Physica B* **192**, 55 (1993).